Journal of
Synchrotron
Radiation

ISSN 0909-0495

Received 23 April 2012
Accepted 16 September 2012

The Debye–Scherrer camera at synchrotron sources: a revisit

Tine Straasø,[a] Jacob Becker,[b] Bo Brummerstedt Iversen[b] and Jens Als-Nielsen[a]*

[a]Niels Bohr Institute, Universitetsparken 5, Copenhagen 2100, Denmark, and [b]Department of Chemistry and iNANO, Center for Materials Crystallography, Langelandsgade 140, Aarhus C 8000, Denmark. E-mail: als@fys.ku.dk

In a powder diffraction pattern one measures the intensity of Miller-indexed Bragg peaks *versus* the wavevector transfer $\sin\theta/\lambda$. With increasing wavevector transfer the density of occurrence of Bragg peaks increases while their intensity decreases until they vanish into the background level. The lowest possible background level is that due to Compton scattering from the powder. A powder diffraction instrument has been designed and tested that yields this ideal low-background level, obtainable by having the space between sample and detector all in vacuum with the entrance window so far upstream that scattering from it is negligible. To minimize overlap of Bragg peaks the combination of fine collimation of synchrotron radiation, a thin cylindrical sample and a high-resolution imaging plate detector is taken advantage of.

© 2013 International Union of Crystallography
Printed in Singapore – all rights reserved

Keywords: powder diffractometer; Compton scattering; charge density; imaging plate detector; peak broadening.

1. Introduction

Powder diffraction of X-rays has been around for almost a hundred years since the seminal work by Debye and Scherrer (Debye & Scherrer, 1916), and today it is probably the most used analytical technique in materials science. A powder diffractogram provides a 'fingerprint' of a crystalline material and it provides a wealth of information (Pecharsky & Zavalij, 2009; Dinnebier & Billinge, 2008). The lattice spacings can be used for phase identification based on database comparison, while the intensity of the Bragg peaks gives access to the crystal structure. Analysis of the peak widths gives insight into the size of the crystalline particles as well as stress and strain in the lattice. In favourable cases when very accurate data are measured it is even possible to determine the three-dimensional electron density distribution in the unit cell of the crystal based on analysis of structure factors extracted from the Bragg intensities (Svendsen *et al.*, 2010).

Powder diffraction data measured with conventional X-ray sources (Pecharsky & Zavalij, 2009; Dinnebier & Billinge, 2008) have the disadvantage of overlapping Bragg peaks at large wavevector transfer $\sin\theta/\lambda$ due to the finite resolution in both the scattering angle 2θ and the wavelength λ. At synchrotron X-ray sources the resolution in both these variables can be squeezed while still retaining sufficient intensity (O'Connor *et al.*, 1997; Fujiwara *et al.*, 2000; Tanaka *et al.*, 2008). For ultimate narrow Bragg widths one can filter the diffracted beams by a set of perfect analyzer crystals (Hodeau *et al.*, 1998; Thompson *et al.*, 2009). However, this requires an angular scan of the analyzer set which significantly increases the time for data collection, and may concomitantly induce radiation damage for crystals of, for example, biogenic origin. We shall not discuss this kind of instrument further in this paper.

If peaks are well resolved then the advantages of powder X-ray diffraction (PXRD) relative to single-crystal X-ray diffraction are that extinction and absorption effects[1] are negligible, and that all Bragg peaks are obtained simultaneously thereby minimizing systematic errors in the assignment of intensity to each reflection. In an important series of papers by Takata and co-workers (Nishibori *et al.*, 2007, and references therein) at the SPring-8 synchrotron laboratory in Japan it has been demonstrated that PXRD data with the appropriate instrument (Nishibori *et al.*, 2001) can provide very accurate data, and these have been used in studies of maximum-entropy-method charge densities of a wide range of materials (Takata *et al.*, 1995; Kitaura *et al.*, 2002). The present work is inspired by the data obtained some time ago from the SPring-8 instrument on β-hematin (Straasø *et al.*, 2011). Synthetic β-hematin and biogenic β-hematin (hemozoin) pose a severe challenge to crystal structure modelling with PXRD since the triclinic unit cell of these poorly diffracting organic crystals contains more than a hundred atoms (including 62 H atoms). We have therefore scrutinized the possibilities for obtaining an improved data set and the present report is the outcome of this work. The most important features are an all-vacuum environment and an energy-dispersive photon

[1] As will be discussed below, the absorption will be measured as part of the line-up procedure.

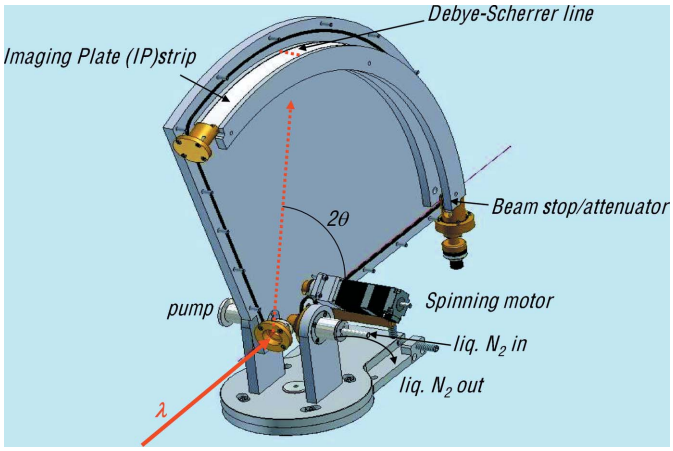

Figure 1
The all-in-vacuum diffractometer. The entrance window of the X-ray beam is further upstream than the figure encapsulates.

counter at 90° enabling a quantitative assessment of the incoherent Compton scattering background. We shall demonstrate that this fundamental low background level can indeed be obtained with a standard reference powder of Si. For general samples, *e.g.* hemozoin crystals, this means that the sample quality in terms of the ratio of crystalline to amorphous phase can be assessed quantitatively as we will report in a forthcoming publication.

Other issues to be discussed here, albeit less prominent, are the precise curvature of the Debye–Scherrer cones intersecting the cylindrical image plate as well as corrections for the time decay of the diffraction patterns recorded on the exposed imaging plate. Based on the general wisdom that one should not fit quantities that can be measured, we determine the zero scattering angle position on the image plate by using a beam attenuator rather than a beam stop, and furthermore we recommend assessing the instrumental width of Bragg peaks without any adjustable fitting parameters[2], which means that the measured widths will directly reflect the grain size and possible strain in the sample.

2. The diffractometer

2.1. Camera and sample mount

The incident monochromatic X-ray beam (red arrow) enters the powder diffractometer canister shown in Fig. 1 (with some parts removed). The powder sample is situated in a thin glass capillary held by a copper collar which can be cooled to approximately 88 K by means of liquid N_2. The beam strikes the capillary ~2 mm from the tip of the collar, thus providing a near-cryogenic sample temperature. Utilizing this sample cooling places a demand on the vacuum level, which must be in the $<10^{-4}$ torr regime in order to quench convective heat transfer to the sample and eradicate ice formation on the capillary. The possibility of sample cooling sets this diffractometer apart from the evacuated Debye–Scherrer camera reported by Sabine and Kennedy (Sabine *et al.*, 1995), in which the vacuum level was 1 torr. The cryoholder furthermore enables free rotation of the sample in the beam as well as appropriate centring of the capillary throughout the rotation. The X-rays enter the diffractometer vacuum through a Kapton window placed several metres upstream. Between the window and the sample one may place a set of in-vacuum guard slits, removing all stray scattering coming from the Kapton. A bellow section in the vacuum tube allows flexible positioning of the diffractometer canister, *e.g.* adjustment of the sample height to the X-ray beam centre.

2.2. Detector systems

The powder diffraction is observed on a Fuji BAS IP SR-2040 imaging plate (IP) strip (shown in white) located on a vertical circular band with a radius of 300 mm and a width of 13 mm. The diffractogram on the strip is read by a GE Typhoon FLA 7000 IP flatbed imaging plate scanner with a 25 µm pixel resolution.[3] The length of an IP strip is 400 mm corresponding to an angular range of 76.4°. The actual diffraction range is broadened by the option of inserting the IP strip at position $2\theta = 0°$ giving the range $0° < 2\theta < 76.4°$ (range #1) or at position $2\theta = 108°$ giving the range $31.6° < 2\theta < 108°$ (range #2). As such, acquiring a full-range diffractogram requires two separate measurements. For many purposes one range is sufficient, especially when using high X-ray energies. The direct beam is also imaged on the IP strip (range #1) after attenuation by several orders of magnitude, so that the position of $2\theta = 0°$ is recorded on the same IP as the powder diffraction Debye–Scherrer lines. In the example discussed below, where data were recorded using a wavelength of 1.054 Å, the attenuation was provided by a 3 mm-long Al rod situated in a 10 mm-long Mo tube acting as a beam catcher. When working at higher energies (*e.g.* 60 keV), Ta may be substituted for Al.

In addition to the imaging plate detector, the diffractometer is equipped with two X-ray photon counters. One is placed at $2\theta = 90°$ where the diffractometer canister has a centred window with a diameter of 14 mm. With this photon counter one can centre the capillary in the X-ray beam using the Compton scattering as the signal. In case the sample contains elements that yield fluorescent X-ray radiation, this detector must be energy dispersive so that one can separate the fluorescent radiation from the Compton scattering. The other photon counter is mounted to measure the transmission of the sample. In order to do so the direct-beam intensity ($\sim 10^{11}$ photons s^{-1}) must be attenuated by $\sim 10^7$. This is done by scattering the beam 90° off a thin Kapton foil into a known small solid angle. The entire system is illustrated in Fig. 2(*a*). Fig. 2(*b*) shows the transmission and scattered beam *versus* sample height on a sample consisting of NIST standard Si powder.

[2] Much in the same spirit as that discussed by Sabine *et al.* (1995).

[3] We do not at present know the point spread function of the IP, and for the FWHM widths we have used the nominal pixel resolution of 25 µm.

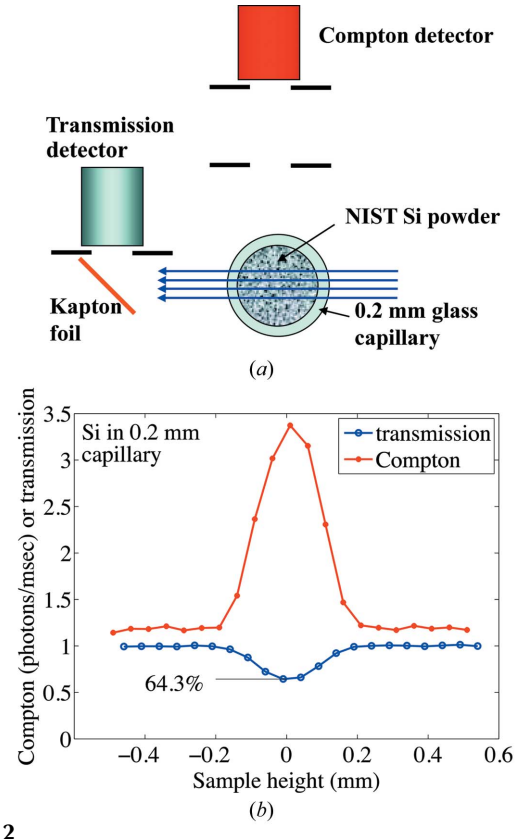

Figure 2
(*a*) Schematic view of the set-up. (*b*) Transmitted and scattered beam *versus* sample height. The transmission of the centred sample is 64.3% and gives the amount of Si powder, which is used to calculate the Compton scattering. The background level of the Compton scattering is due to air scattering as the diffractometer was not evacuated during measurement.

3. Diffraction pattern from a standard Si powder

3.1. Experimental information

To demonstrate the data quality from the all-in-vacuum diffractometer, PXRD data were recorded on a reference powder sample of silicon (NIST) at beamline I911-1 at MAX-lab, Sweden. The Si powder was packed in a 0.2 mm Lindemann capillary. The monochromatic beam (λ = 1.054 Å) was obtained from a diamond crystal in asymmetric (111) Laue geometry situated 9 m from the wiggler source. It was focused in the vertical direction by a curved multilayer mirror placed 4 m upstream from the sample. The beam was apertured down to dimensions of 0.05 mm × 0.1 mm (vertically and horizontally), 300 mm upstream from the sample. The data were recorded at room temperature.

3.2. Determination of the zero point for the Bragg angle

The pixel pattern on the IP strip encompassing the innermost nine Si reflections is shown on a logarithmic intensity scale in Fig. 3. The incident beam profile, attenuated by 3 mm of Al encapsulated in a 10 mm-long tube of Mo, acting as a beam catcher, is shown in the right-hand lower part on a linear scale. Note the different range of pixels in the horizontal and vertical directions. One pixel is 25 µm × 25 µm.

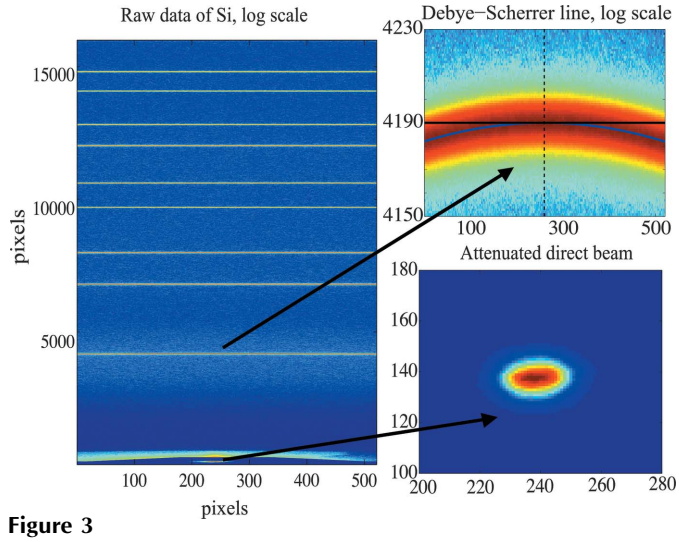

Figure 3
The IP pixel pattern along the Debye–Scherrer (DS) rings appearing as almost straight lines in the left-hand panel, with logarithmic intensity colour scale. In the upper right-hand panel the innermost DS ring is shown on an expanded pixel scale, and with logarithmic intensity colour scale. The calculated DS footprint (blue line) is explained in further detail in §3.3 and in Appendix *A*. The lower right-hand panel shows the attenuated direct beam spot on an expanded pixel scale with linear colour scale.

3.3. Summation along the Debye–Scherrer rings

In order to assign intensity to a given (*hkl*) Bragg reflection one must sum the intensities of pixels along the Debye–Scherrer (DS) footprint on the IP strip. A numerical procedure for obtaining the DS footprint is given in Appendix *A*. The result depends on the scattering angle 2θ and is shown for four different scattering angles (blue lines) in Fig. 4. The deviation from circular increases as a function of scattering angle (circular approximation shown by red dots). The green

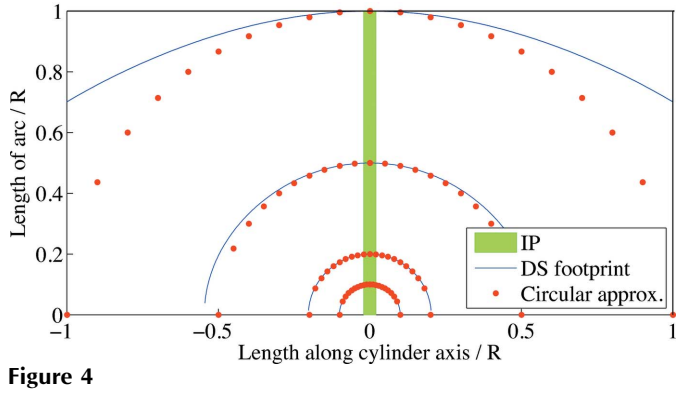

Figure 4
Footprint curves in the plane of the IP, folded out to be flat. Different curves represent different scattering angles in radians. The full line (blue) is the numerical calculation and red dots represent the circular approximation. The curves are at 0.1, 0.2, 0.5 and 1 rad. When the opening angle of the cone approaches π the footprint approaches a straight line. The IP strip in the present case is shown in green (the width of the IP is 13 mm and the radius *R* of the camera is 300 mm).

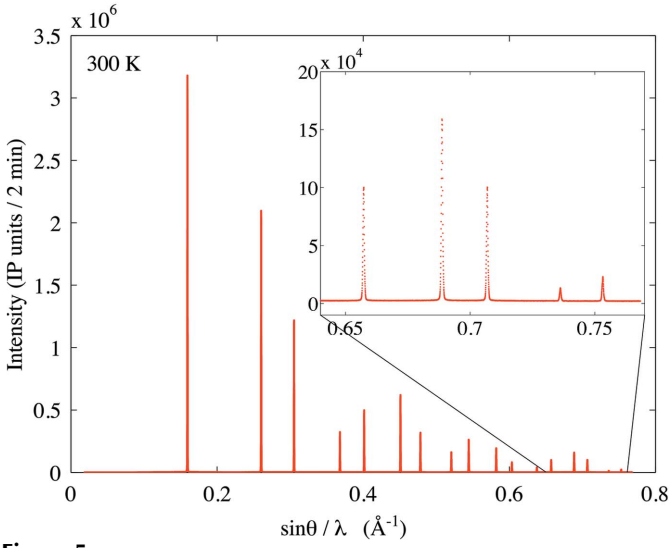

Figure 5
Diffraction pattern from a reference powder sample of silicon (NIST) using the all-in-vacuum diffractometer at an X-ray wavelength λ = 1.054 Å from beamline I911-1 at MAX-lab.

area represents the IP strip of this camera. One such curve is marked in blue in the Si data set for $2\theta = 19.35°$ in Fig. 3 (upper right). The proper summation over pixels for each DS apex angle $u = 2\theta$ then provides the conventional powder pattern as shown in Fig. 5.

3.4. Width of the DS lines

There are six contributions to the width of the DS lines as shown in the upper part of Fig. 6. The contribution from the finite particle size D is $\Delta_{2\theta,\mathrm{par.\,size}} = (\lambda/D)/\cos\theta$. The standard Si powder from NIST had an average grain size D of ~1 µm. By differentiating Bragg's law one finds that a relative wavelength band of $\Delta\lambda/\lambda$ implies a divergence of the scattered beam of $\Delta_{2\theta,\mathrm{hor.\,div.}} = 2\tan\theta(\Delta\lambda/\lambda)$. In the present set-up a monochromatic beam was extracted from the synchrotron beam by Bragg scattering from a diamond monochromator crystal in the horizontal direction, and thus the relative wavelength band is $\delta_h/\tan\theta_M$ with δ_h being the incident horizontal divergence of the synchrotron beam.[4] The monochromatic beam was focused in the vertical plane by a curved mirror, providing a divergence on the sample of $\Delta_{2\theta,\mathrm{ver.\,div.}} = 2\delta_v$. The last three contributions are due to the apparent capillary width as seen along the beam direction, the finite beam height and the finite pixel size. All of the contributions are added in quadrature and δ_h and δ_v are fitted to 0.366 mrad and 0.330 mrad, respectively. If δ_h and δ_v are known, this procedure will, compared with profile fitting, minimize the number of parameters to be fitted, thus allowing for a better determination of the structural parameters.

[4] In principle the beam divergence parameters δ_h and δ_v should be measured. Unfortunately the means for this was not available during the experimental time at the beamline at MAX-lab, but the values in Fig. 6 are quite reasonable estimates. The finite Darwin width of the monochromator crystal can be neglected here in evaluating $\Delta\lambda/\lambda$.

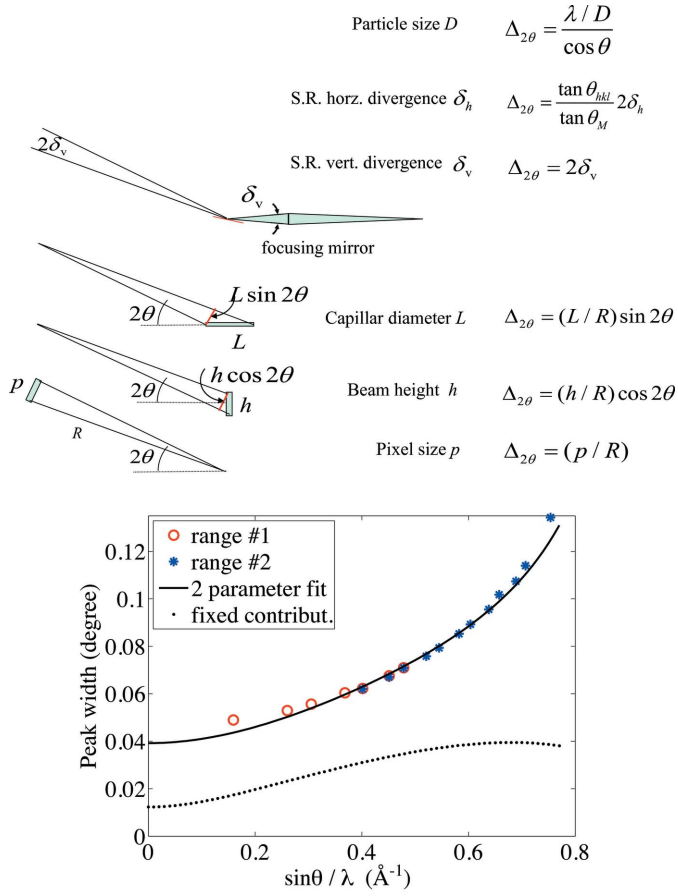

Figure 6
There are six contributions to the width of a powder line as depicted in the upper part of the figure and explained in the text. The experimentally derived widths from range #1 and range #2 are shown in red and blue markers, respectively. The full line in the graph shows the resulting width using δ_h = 0.366 mrad and δ_v = 0.330 mrad, and the dotted line shows the remaining fixed contributions.

3.5. Compton scattering background level

In this experiment a 0.05 mm-high monochromatic X-ray beam is incident on a horizontal glass capillary with a nominal diameter of 0.2 mm and a glass wall thickness of 0.01 mm. The capillary may be empty, or it may be filled with a sample powder, in this case silicon characterized by NIST. The transmitted and Compton-scattered X-rays are measured with the photon counters as previously described (Fig. 2). The widths of the curves are consistent with a capillary outer diameter of 0.2 mm. The scattered beam is primarily Compton scattering on a flat background of the scattering from air since the diffractometer canister was not evacuated during this measurement. The transmission when the capillary is centred in the beam is 64.3%. At a wavelength of 1.054 Å the calculated transmission is 95.2% for 0.02 mm glass and 67.3% for 0.085 mm solid Si, giving a total transmission as measured. This means that the powder density is 0.085/(0.200 − 0.020) = 47% of solid Si, a typical value for powder samples. The electron density in Si is about 6% higher than in SiO_2, so the Compton scattering from Si will be 1.06(0.085/0.020) times larger than that from the empty glass capillary.

Fig. 7(*a*) shows the full scattering profile in terms of $\sin\theta/\lambda$ from the empty glass capillary. The Compton, or incoherent, fraction of the scattering *versus* $\sin\theta/\lambda$ can be evaluated from data from the *International Tables of Crystallography*. At the highest values of $\sin\theta/\lambda = 0.7$ Å^{-1}, about 76% is Compton scattering and 24% is coherent scattering. One can thus calculate the Compton scattering at all values of $\sin\theta/\lambda$, as shown by the red curve, and one can generate the incoherent scattering from the Si powder by using the ratio of thickness and electron density relative to glass as shown by the dotted red curve. However, with Si powder in the glass capillary, the beam will be attenuated by a factor of 0.643 as shown in Fig. 2(*b*). Taking this attenuation into account, the total background scattering consisting of glass scattering and incoherent scattering from Si can be calculated, and this is shown as the green line.

In Fig. 7(*b*) the full diffraction profile from the Si powder in terms of $\sin\theta/\lambda$ is shown on a logarithmic intensity scale. The level in-between the powder lines is consistent with the background curve calculated as described above, without any adjustable parameters. The light green bar indicates the region seen by the photon counter mounted at $2\theta = 90°$.

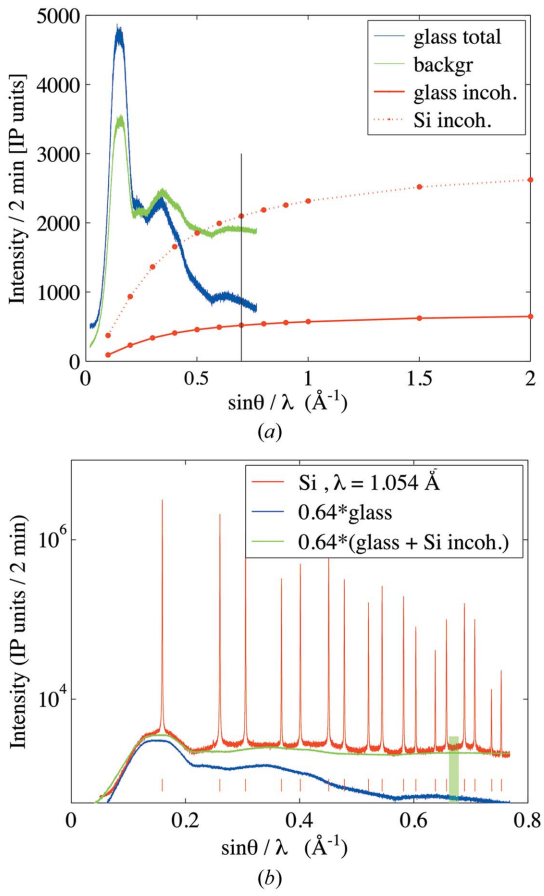

Figure 7
(*a*) Scattering profile of the empty glass capillary (blue). The calculated incoherent scattering fraction at $\sin\theta/\lambda = 0.7$ is 76% for glass and 69% for Si. The corresponding incoherent intensities are shown in red (glass, full line; Si, broken line; neglecting absorption). The green line shows the total background level consisting of the sum of the glass capillary and the incoherent scattering from Si, multiplied by the transmission of 0.643 owing to the absorption from the Si powder. (*b*) The scattering profile of Si is shown in red and the background as determined from (*a*). The green semi-transparent box indicates the region seen by the photon detector mounted at $2\theta = 90°$.

4. Time decay and sensitivity of the imaging plate

There are two issues to be addressed when using an imaging plate as detector. The first is the decay or fading of the signal from the exposed IP (*cf.* Amemiya, 1995). As image plates and the laser reading equipment are developed over time, we determined the appropriate time constants experimentally by irradiating different areas of the IP at different times with the same X-ray beam. The registered intensities are shown in Fig. 8 (blue dots) together with a fitted algorithm for the decay times (blue line). The exposure time was 10 s, short enough to neglect any decay during the exposure.

Depending on the nature of the sample the general exposure time will be considerably longer, somewhere between 2 and 30 min. In that case the decay during exposure cannot be neglected. Furthermore, the decay continues during development and would lead to incorrect relative intensities, if not accounted for. A virtual example will serve to illustrate how the data should be corrected for decay. In the virtual example the IP was exposed for 8 min (red line, Fig. 8) and developed for 4 min (black line) after a waiting period of 10 min. During exposure, the data have decayed for 8/2 = 4 min on average. The scanner reads the IP strip from the low 2θ end towards the high 2θ end. Pixel values at the lowest 2θ are thus corrected as to a time decay of 8/2 + 10 = 14 min, while the pixel values at the highest 2θ as to a time decay of 8/2 + 10 + 4 = 18 min. The intermediate data points are corrected according to their relative 2θ values.

The second issue is the sensitivity, *i.e.* conversion of IP units to photons (Amemiya, 1995). When analysing diffraction data

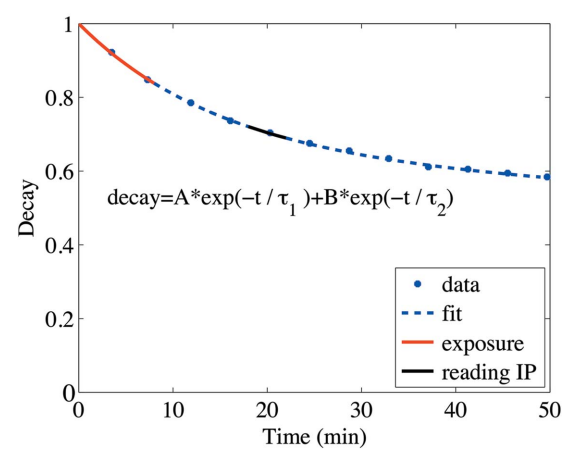

Figure 8
Measured data showing the decay in the IP and the fitted decay times in blue. The fitted parameters have the following values: $A = 0.36$, $B = 0.64$, $\tau_1 = 14.9$ min and $\tau_2 = 434$ min. The plot furthermore illustrates a virtual example, where the IP is exposed for 8 min (red), waiting for 10 min and developed for 4 min (black). The correct decay correction is explained in the main text.

by fitting to structure models, it is important that the statistical accuracy is correctly assessed, *e.g.* by converting IP units to photon counts obeying Poisson statistics. From Fig. 2(*b*) one can obtain an intensity of Compton scattering from the Si-filled capillary of 2188 photons s^{-1} through a 14 mm-diameter aperture at a distance of 300 mm from the sample, *i.e.* at scattering angles in the range $90^\circ - 1.33^\circ$ to $90^\circ + 1.33^\circ$ corresponding to the vertical semi-transparent green box in Fig. 7(*b*). On the other hand, the IP strip in this scattering angle region near 90° contained no Bragg lines, and when integrated over the area of $(\pi/4)14^2$ mm^2 it yielded 9760 IP units per second. Therefore the conversion factor is about 4.5 IP units per X-ray photon.

5. Signal to noise of weak Bragg peaks

In Fig. 9 the data obtained with the all-in-vacuum instrument (red curve) are compared with the data of Nishibori *et al.* (2007) (including the provided supplementary information). The outermost obtainable data at an X-ray energy of 11.8 keV were in the region of $\sin\theta/\lambda$ near 0.75 $Å^{-1}$. The registered intensities are shown on a logarithmic scale. The signal-to-noise ratio for the peak at $\sin\theta/\lambda = 0.707$ $Å^{-1}$ is about 40 for the red curve but 10 for the blue curve. The ratio of the widths is about 1:2. The background level of the all-in-vacuum data (green line) is fully accounted for by Compton scattering without any adjustable parameters. A detailed comparison of all-in-vacuum data with that of Nishibori should ideally be made on the same beamline at the same wavelength, but it seems obvious that the quality of the all-in-vacuum data is qualitatively superior.

Another illustration is provided by comparison of very weak Bragg peaks such as the 'forbidden' (222) reflection. When the electron charge distribution is approximated by the spherical symmetric electron cloud in the free Si atom, the (222) reflection is strictly forbidden. However, there are two effects invalidating this approximation. One is the chemical bonding to the neighbouring atoms, and the other is the anharmonic vibrations of the atoms. As shown by Roberto & Batterman (1970), these two effects are partly cancelling each other out. At low temperatures the anharmonic vibrations are insignificant and the chemical bonding is the dominant mechanism, whereas at high temperatures the anharmonic vibration is the dominant effect. It turns out that in Si at room temperature the two effects almost cancel each other out, and this makes the (222) reflection very weak. The powder diffraction data of Nishibori *et al.* (2007) yielded an intensity ratio of 0.01% between the (222) and the (111) reflection. The all-in-vacuum data in Fig. 5 yield a peak intensity of the (111) reflection of 3.2×10^6/2 min, whereas the (222) reflection shown in Fig. 10 gives 300/2 min, indeed in accordance with the result of Nishibori *et al.* Visual inspection demonstrates that this very weak Bragg reflection is qualitatively more clearly observed in the all-in-vacuum instrument.

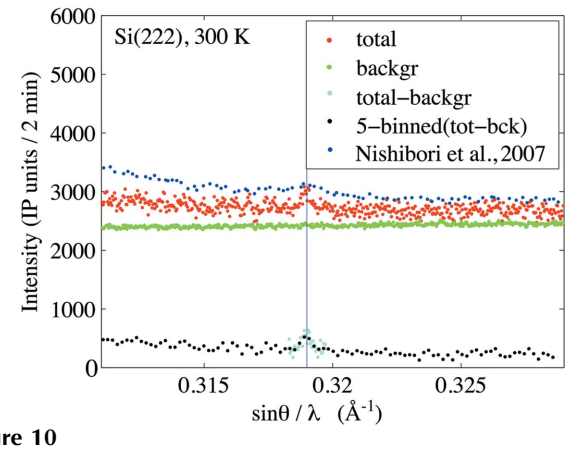

Figure 10
Observation of the 'forbidden' (222) reflection at the calculated position shown by the blue vertical line. The intensity is about four orders of magnitude lower than the allowed (111) reflection. To visualize that the signal outside the peak region is a smooth curve the data have been binned in blocks of five (black dots). Within the region of the peak (cyan dots) the fine graining is maintained. The blue data points are from Fig. 2 of Nishibori *et al.* (2007) but scaled by 0.25 to obtain the same statistics.

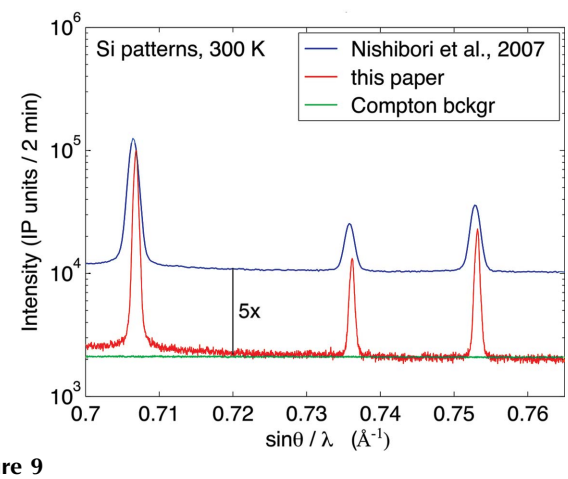

Figure 9
Comparison of data taken with the all-in-vacuum diffractometer (red curve with the green curve showing the Compton background) and the data of Nishibori *et al.* (2007) shown as the blue curve. The signal-to-noise ratio is significantly better with the all-in-vacuum diffractometer.

6. Summary and outlook

A Debye–Scherrer camera with an imaging plate detector receiving highly collimated and monochromated X-rays from a synchrotron source is described. Special attention has been given to minimize the background, and to quantitatively assess the Compton scattering by introducing an energy-dispersive photon counter, which also serves conveniently for aligning the sample and for determination of the packing fraction of the powder. In addition, proper summation over pixels in each Debye–Scherrer ring is discussed, as well as corrections for the time decay in the imaging plate during exposures. It is evident from Fig. 5 that Bragg peaks are observable up to considerably larger values of $\sin\theta/\lambda$ than 0.8 $Å^{-1}$ if one uses harder X-rays than 11.8 keV. With the combination of a hard X-ray energy synchrotron beam and the present low-background instrument, it will be possible to record structure factors out to $\sin\theta/\lambda$ around 2 $Å^{-1}$ and thus open up the opportunity of

a whole new dimension of chemical bonding studies with experimental access to the core electron distribution.

APPENDIX *A*
Intersection of the Debye–Scherrer cone with the imaging plate

The incident monochromatic X-ray beam (black line in Fig. 11) is horizontal and hits the powder sample located at O. The imaging plate detector (pink) is curved as a cylinder with horizontal axis perpendicular to the incident beam. The Bragg-scattered rays for a given set of Miller indices are distributed over the Debye–Scherrer cone, indicated by the blue lines, and intercept the imaging plate along the green line. The uppermost Bragg-scattered ray terminates on the imaging plate at A and the corresponding Debye–Scherrer circle is AQB, spanning an azimuthal angle of 90°. The ray OQ at an arbitrary azimuthal angle φ has the same length as OA. Thus OQ does not terminate on the imaging plate, but, expanding it to be OP by the factor f, *i.e.* $f \cdot \mathbf{OQ} = \mathbf{OP}$, P will be on the image plate, so by determining the coordinates of P one generates the green trace on the image plate. Taking the image-plate cylinder radius as the unit of length, the explicit coordinates of Q is

$$Q = \left\{\left[1 - (\sin u \sin\varphi)^2 - (\sin u \cos\varphi)^2\right]^{1/2}, \sin u \sin\varphi, \sin u \cos\varphi\right\},$$

where u is twice the Bragg angle.

The coordinates of P, being on the cylinder surface, must obey $x_p^2 + z_p^2 = 1$, *i.e.*

$$f^2\left[1 - \sin^2 u \sin^2\varphi\right] = 1 \qquad \text{or}$$

$$f(u, \varphi) = 1/\left[1 - \sin^2 u \sin^2\varphi\right]^{1/2}.$$

The final result is then

$$P = \left\{\left[1 - (\sin u \sin\varphi)^2 - (\sin u \cos\varphi)^2\right]^{1/2}, \sin u \sin\varphi, \sin u \cos\varphi\right\} \Big/ \left[1 - \sin^2 u \sin^2\varphi\right]^{1/2}.$$

The diffractometer was designed by the late J. Linderholm from the company JJ-X-ray, and produced, assembled and modified in several stages by H. Bro Pedersen at JJ-X-ray with funding from the Carlsberg Foundation. Initial tests took place at the Swiss Light Source, optics beamline X05A, and we thank the staff for beam time and assistance. The cooling system was developed in the Chemistry Department at Aarhus University with substantial and devoted help from Palle Kjær Christensen. We thank The Danish National Research Foundation (Center for Materials Crystallography) and the Danish Strategic Research Council (Center for Energy Materials) for additional support.

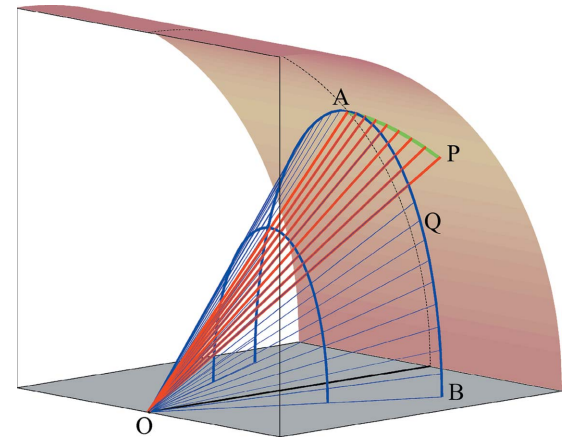

Figure 11
Intersection of the Debye–Scherrer cone with the imaging plate. See text for details.

References

Amemiya, Y. (1995). *J. Synchrotron Rad.* **2**, 13–21.
Debye, P. & Scherrer, P. (1916). *Phys. Z*, **17**, 277–283.
Dinnebier, R. E. & Billinge, S. J. L. (2008). *Powder Diffraction, Theory and Practise*, 1st ed. Cambridge: RSC Publishing.
Fujiwara, A., Ishii, K., Watanuki, T., Suematsu, H., Nakao, H., Ohwada, K., Fujii, Y., Murakami, Y., Mori, T., Kawada, H., Kikegawa, T., Shimomura, O., Matsubara, T., Hanabusa, H., Daicho, S., Kitamura, S. & Katayama, C. (2000). *J. Appl. Cryst.* **33**, 1241–1245.
Hodeau, J.-L., Bordet, P., Anne, M., Prat, A., Fitch, A. N., Dooryhee, E., Vaughan, G. & Freund, A. (1998). *Proc. SPIE*, **3448**, 353–361.
Kitaura, R., Kitagawa, S., Kubota, Y., Kobayashi, T. C., Kindo, K., Mita, Y., Matsuo, A., Kobayashi, M., Chang, H. C., Ozawa, T. C., Suzuki, M., Sakata, M. & Takata, M. (2002). *Science*, **298**, 2358–2361.
Nishibori, E., Sunaoshi, E., Yoshida, A., Aoyagi, S., Kato, K., Takata, M. & Sakata, M. (2007). *Acta Cryst.* A**63**, 43–52.
Nishibori, E., Takata, M., Kato, K., Sakata, M., Kubota, Y., Aoyagi, S., Kuroiwa, Y., Yamakata, M. & Ikeda, N. (2001). *Nucl. Instrum. Methods Phys. Res. A*, **467**, 1045–1048.
O'Connor, B. H., van Riessen, A., Carter, J., Burton, G. R., Cookson, D. J. & Garrett, R. F. (1997). *J. Am. Ceram. Soc.* **80**, 1373–1381.
Pecharsky, V. K. & Zavalij, P. Y. (2009). *Fundamentals of Powder Diffraction and Structural Characterization of Materials*, 2nd ed. New York: Springer.
Roberto, J. B. & Batterman, B. W. (1970). *Phys. Rev. B*, **2**, 3220–3226.
Sabine, T. M., Kennedy, B. J., Garrett, R. F., Foran, G. J. & Cookson, D. J. (1995). *J. Appl. Cryst.* **28**, 513–517.
Straasø, T., Kapishnikov, S., Kato, K., Takata, M., Als-Nielsen, J. & Leiserowitz, L. (2011). *Cryst. Growth Des.* **11**, 3342–3350.
Svendsen, H., Overgaard, J., Busselez, R., Arnaud, B., Rabiller, P., Kurita, A., Nishibori, E., Sakata, M., Takata, M. & Iversen, B. B. (2010). *Acta Cryst.* A**66**, 458–469.
Takata, M., Umeda, B., Nishibori, E., Sakata, M., Saito, Y., Ohno, M. & Shinohara, H. (1995). *Nature (London)*, **377**, 46–49.
Tanaka, M., Katsuya, Y. & Yamamoto, A. (2008). *Rev. Sci. Instrum.* **79**, 075106.
Thompson, S. P., Parker, J. E., Potter, J., Hill, T. P., Birt, A., Cobb, T. M., Yuan, F. & Tang, C. C. (2009). *Rev. Sci. Instrum.* **80**, 075107.